nature communications

Article

https://doi.org/10.1038/s41467-025-64875-0

Achieving electrochemical and mechanical stability in a lightweight titanium alloy

Received: 13 February 2025

Accepted: 29 September 2025

Published online: 12 November 2025

Check for updates

Jixun Zhang[1,2,6], Jianyang Zhang[1,3,6], Weicheng Xiao[1], Xier Luo[1], Xia Li[1], Na Li[1], Hong Luo[4], Peter K. Liaw[5] & Tao Yang[1,2,3]

Titanium alloys represent a promising material in marine applications, focusing on high-stakes environments where their corrosion resistance and high specific strength offer significant benefits. However, they can still be vulnerable to localized corrosion, such as pitting corrosion and stress corrosion cracking, in the presence of aggressive chlorides. Here we report a lightweight titanium alloy that addresses these issues through conventional casting and thermal-mechanical processing. The alloy can generate a passive film showing distinct but stable electrochemical responses. It is found that the reaction of the passive film can shift from the slow accumulation in the passive region, to the rapid buildup of passive layers in extreme anodic potentials. Consequently, the alloy exhibits a pitting potential above 10 VSCE without being subjected to localized corrosion. Meanwhile, mechanical reliability is also achieved during stress corrosion tests, owing to the fast repair of the passive film that substantially constrains the crack propagation. Such virtual immunity to seawater corrosion qualifies this titanium alloy as a potential candidate for long-term cost savings and sustainability.

Titanium alloys have outstanding application prospects in various industries ranging from aerospace to marine engineering, offering the advantages of high specific strength and corrosion resistance. Their weight-saving feature is crucial to meet the global demand for economic efficiency, which however, is challenged by material degradation due to environmental corrosion during their practical service[1–4]. Among various service conditions, seawater is the most common and global environment where corrosion, erosion, and maintenance remain the primary concern[5,6]. Compared with other major alloy classes, titanium alloys demonstrate higher resistance to seawater, attributed to the high affinity between titanium and oxygen[7,8]. Nowadays, titanium alloys are playing important parts in the marine industry, driven by the economic benefits of service reliability and reduced maintenance. For structural use, such as shipbuilding and naval technologies where high strength and corrosion resistance are of decisive importance, state-of-the-art Ti alloys, including TC4, TC4 ELI, and PT-3V, are increasingly used in the construction of marine objects[9–11]. For functional applications, titanium and its alloys, including pure Ti, TC4, and Ti-Pd, are leading candidates in technologies like heat exchangers for ocean thermal energy conversion, offering plant lifespans exceeding 30 years[12–14]. As titanium alloys are gaining significant proportion in marine industries, a major cost can be saved by improving the corrosion resistance, thereby reducing or eliminating corrosion-related maintenance issues[15].

The primary corrosion challenges faced by titanium alloys include pitting corrosion, galvanic corrosion, and stress corrosion cracking (SCC)[7,16]. Titanium alloys are electrochemically susceptible to aggressive environments with high halide concentrations, such as seawater with elevated chloride ion (Cl^-) levels that promote the localized dissolution of passive films on the alloy surface[17,18]. This process results in

[1]Department of Materials Science and Engineering, College of Engineering, City University of Hong Kong, Hong Kong, China. [2]Hong Kong Branch of National Precious Metals Material Engineering Research Centre (NPMM), City University of Hong Kong, Hong Kong, China. [3]Centre for Advanced Structural Materials, City University of Hong Kong Shenzhen Research Institute, Shenzhen, China. [4]National Materials Corrosion and Protection Data Center, Institute for Advanced Materials and Technology, University of Science and Technology Beijing, Beijing, China. [5]Department of Materials Science and Engineering, University of Tennessee, Knoxville, USA. [6]These authors contributed equally: Jixun Zhang, Jianyang Zhang. e-mail: taoyang6-c@my.cityu.edu.hk

high pitting susceptibility of alloys, such as the commercial TC4 and NiTi alloys[19–22], which is generally considered the main failure mode of corrosion in aggressive environments[23]. Electrochemical corrosion can also be accelerated by galvanic corrosion, especially in titanium alloys with dual β and α structures to form galvanic cells[7,24]. Additionally, materials in deep-sea environments inevitably have significant risks of SCC due to the combined effect of high hydrostatic pressure and corrosive conditions. The nucleation and propagation of microcracks under SCC compromise the reliability of materials and eventually lead to catastrophic fractures[25,26]. Titanium alloys and other commercial alloy classes, including stainless steels, aluminum alloys, and bronzes, have been demonstrated to be susceptible to SCC in seawater[3,7,27–31]. Mechanical performance influenced by SCC often exhibits reduced strength and ductility, leading to unpredictable structural failure and making this vulnerability a very crucial issue. Therefore, improving the anti-corrosion performance and SCC resistance of titanium alloys means the benefits of long-term service cost economy and reliability[7,12].

In the present work, we developed a lightweight titanium-based alloy ($Ti_{82.19}V_{12.5}Al_{3.5}Fe_{0.8}Hf_1B_{0.01}$, at.%) with a mass density of ~4.72 g/cm^3 and a chemically homogeneous triple-phase structure to enhance both electrochemical and mechanical stability. The alloy exhibited distinct but stable electrochemical behavior in the seawater-like solution (3.5 wt.% NaCl solution) during potentiodynamic polarization tests. The passive film was observed to slowly accumulate from several nanometers to tens of nanometers in the passive region. When the polarization reached the second passive region with extreme anodic potentials, the reaction shifted to the rapid buildup of passive layers, eventually forming a protective barrier with a thickness of ~600 nm coated on the alloy surface. Such resilient passivation enabled excellent electrochemical stability of the alloy, giving rise to an unprecedented pitting resistance above 10 V_{SCE}. More importantly, due to its rapid passivation ability, the alloy also exhibited strong resistance to SCC in 3.5 wt.% NaCl solution. Microcracks nucleated but their propagation was substantially constrained, retaining the alloy's tensile strength with minimal loss of ductility. This remarkable synergy of electrochemical and mechanical stability will enhance the robust application of this titanium alloy in marine industries.

Results and Discussion

Microstructure of the TiV-based alloy

We first fabricated the TiV-based alloy with a refined grain structure through multi-step processing of cold rolling and intermediate annealing. To minimize the impact of chemical discontinuities that can promote localized corrosion, we designed a metastable β-Ti comprising other athermal phases. As shown in Fig. 1a, the alloy has a dual-phase structure consisting of the β-Ti and α" martensite phases. It can be seen that equiaxed β-Ti grains and the needle-shaped α" plates constitute the basic microstructural morphology of the material (Fig. 1b–d). When examined using transmission electron microscopy (TEM), in addition to the typical β and α" phases (Fig. 1e), athermal ω precipitates were also revealed and found dispersing evenly in the β phase matrix (Fig. 1f, g). The ω phase was introduced during the quenching process associated with the athermal transformation, suggesting the absence of galvanic cells that could promote the localized dissolution of passive films. This is evidenced in the energy dispersive spectrometer (EDS) mapping in Fig. 1h, where no distinct elemental segregation is found in ω particles[7,24,32].

Resistance to electrochemical corrosion

Figure 2a shows the potentiodynamic polarization curve of the TiV-based alloy in 3.5 wt.% NaCl solution, with the commercial TC4 (Grade 5) and NiTi ($Ni_{50.6}Ti_{49.4}$, at.%) alloys displayed for comparison. The TiV-based alloy has slightly lower corrosion potentials (E_{corr}) compared to the TC4 alloy but is higher than that of the NiTi alloy. In terms of current density, however, it can be seen that the TiV-based alloy is most distinguished by having the lowest corrosion current density (i_{corr}) as well as much reduced passivation current density (i_{pass}) during the passive region, suggesting its much slower corrosion rate[33]. Following the passive region, the NiTi and TC4 alloys exhibit low pitting potential (E_{pit}) of ~0.2 V_{SCE} and ~1.7 V_{SCE}, respectively. This is attributed to the early breakdown of the passive film and accordingly, corrosion pits are observed on the surface of NiTi and TC4 alloys, confirming their deteriorated localized corrosion (Supplementary Fig. 1)[34]. In strong contrast, the passive region of the TiV-based alloy extends to ~4.5 V_{SCE} and is then followed by a second passive region with superb electrochemical stability. During the second passive region, the current density restores ultimate stability and is maintained at a very stable value, without exhibiting any pitting or metastable pitting behavior throughout the polarization process. Consequently, the alloy demonstrates an unprecedented pitting resistance above 10 V_{SCE}. As shown in Fig. 2b, in addition to the very low value of i_{corr}, the pitting resistance of the TiV-based alloy shows a substantial advantage over other existing alloy classes for marine applications, such as Ti alloys[19,35–37], stainless steels[38–41], Ni-based alloys[42,43], metallic glasses[44,45], Al alloys[46,47], Cu alloys[48,49], and high entropy alloys[50–56]. Such electrochemical stability suggests the compact characteristic of the passive film and its stable growth during the electrochemical corrosion process. As the passive film grew and thickened, it became macroscopically visible and eventually coated on the alloy surface, without forming any pit that accelerated localized corrosion (Fig. 2c). This virtual immunity to seawater holds great potential for long-term service in marine or other aqueous environments. Details for the electrochemical parameters, including E_{corr}, i_{corr}, and E_{pit}, are summarized in Table 1.

To unveil underlying reasons associated with the superior corrosion resistance in the TiV-based alloy, we subsequently studied the impedance behavior of the three alloys after open circuit potential (OCP) stabilization (Supplementary Fig. 2). In addition to the typical impedance features that support the superior corrosion resistance in the TiV-based alloy (e.g., the substantially larger Nyquist semicircle, higher phase angle, and more ideal capacitive response), simulated impedance behavior and the fitting results show that the TiV-based alloy has an electrical equivalent circuit (EEC) with only one time-constant, representing a monolayer of the compact passive film[57,58] (Supplementary Fig. 3). The EECs of the TC4 and NiTi alloys, on the other hand, are made of multi-layers structures that generally include outer porous layers[59,60]. According to the electrochemical impedance spectroscopy (EIS) fitting results in Supplementary Fig. 2 and Supplementary Table 1, the passive film resistance (R) of the TiV-based alloy is at least one order of magnitude higher than that of the TC4 and NiTi alloys, indicating its more protective (electrochemically stable) film. Therefore, it is suggested that the structural difference and resistance of passive films contribute to the distinct electrochemical behavior of the three alloys. Details of the impedance behavior and simulation are discussed in Supplementary Note 1.

To our knowledge, few literature reports any alloy capable of withstanding anodic potential up to 10 V_{SCE} in 3.5 wt.% NaCl without suffering localized corrosion. Correspondingly, there is a very limited understanding of how the passive film reacts to extreme corrosion potentials. Aiming to study the passive film development during the electrochemical corrosion process, we first carried out TEM investigation to elucidate the structure of the passive film. Figure 3a shows a typical high-resolution TEM (HRTEM) of the sample potentiodynamically polarized to 2 V_{SCE}, revealing detailed structural information about the passive film and its adjacent layers. According to the contrasts of different layers and their corresponding fast Fourier transform (FFT) patterns, four well-characterized layers containing the β-Ti matrix, passive film, and nanocrystalline Au/Pt layers can be identified (Fig. 3b). The beam direction was taken along $<0\,0\,1>_{\beta}$, showing a clear

https://doi.org/10.1038/s41467-025-64875-0

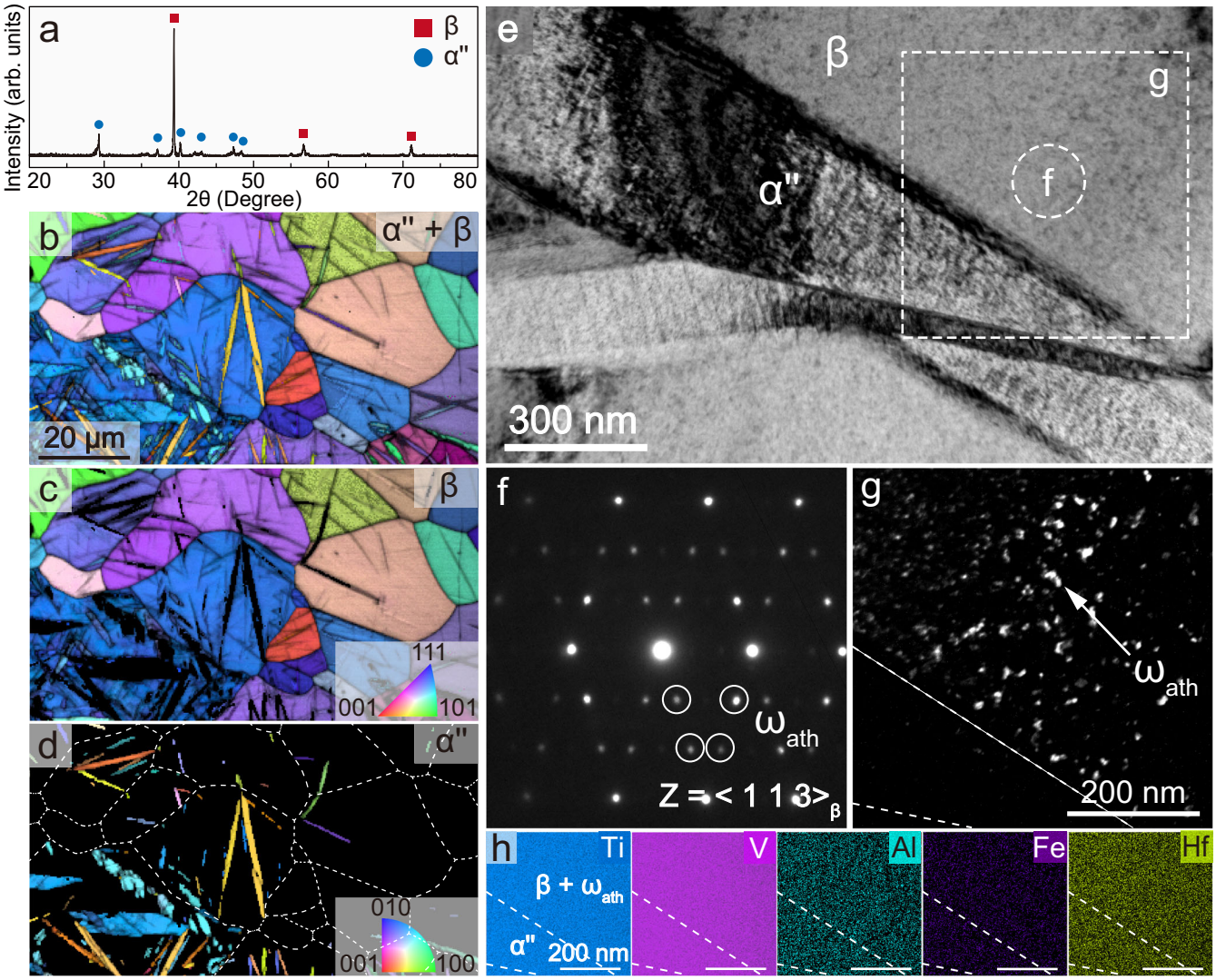

Fig. 1 | Microstructure of the TiV-based alloy. a X-ray diffraction (XRD) spectrum. **b**–**d** Electron back-scattered-diffraction (EBSD) images (inverse pole figure (IPF) and image quality (IQ)) showing the overview of microstructures. The average confidence index (CI) for (**b**–**d**) is 0.5087, 0.5715, and 0.1886, respectively. **e** TEM bright-field (BF) image. **f** Selected area electron diffraction (SAED) of the area marked by the dashed circle in (**e**). **g** TEM dark-field (DF) image of the area marked by the dashed square in (**e**), highlighting the distribution of athermal ω precipitates. **h** EDS mapping of (**g**) showing compositional homogeneity of the material. Source data for (**a**) are provided as a Source data file.

crystallographic arrangement of the β-Ti matrix. An amorphous layer with a thickness of ~10 nm, attaching to the β-Ti substrate, is identified as the passive film. The amorphous characteristic of the passive film is due to the massive dissolution of oxygen atoms, resulting in the loss of crystallographic information compared to the perfectly periodic arrangement in the β-Ti matrix[61].

Having understood the amorphous characteristic of passive films, we next conducted detailed investigations on the evolution of passive films, which were potentiodynamically polarized to various potentials ranging from 1 V_{SCE} to 10 V_{SCE}. Figure 3c shows the TEM BF images of passive films anodically polarized to different potentials, revealing their steady growth with the increasing potential. At the early stage of the passive region (such as 1 V_{SCE}), the passive film had a thickness of ~5 nm. When the polarization potential rose to 3 V_{SCE}, the passive film thickness slowly grew to ~30 nm. Remarkably, as the corrosion process reached the second passive region at the potential of 6 V_{SCE}, the passive film was piled up to ~360 nm, which was found to build up layer by layer. The result suggests that the rapid buildup of the passive layers can prevent the breakage of the passive barrier at high anodic potential, thereby suppressing the occurrence of localized corrosion. Ultimately, the passive film thickness grew to ~600 nm as the corrosion potential reached 10 V_{SCE}, with its characteristic layered structure remaining intact, indicating its superb electrochemical stability. The elemental distribution in Supplementary Fig. 4 shows a clear enrichment of O and a small amount of Ti and V in the passive layers, forming a thick barrier of Ti/V oxides coated on the matrix to protect against the high-potential corrosive environment. Figure 3d shows the statistical histogram of the passive film thickness at various polarization potentials. It can be seen that the passive film thickened slowly during the first passive region, and then accumulated dramatically during the second passive region. The result suggests that the pitting corrosion is prevented by the resilient electrochemical responses, from the steady growth of the passive film during the first passive region, to the rapid buildup of passive layers in the second passive region. Consequently, the passive films exhibit different morphologies, from the uniform passive film to the layer-structured passive barrier. We subsequently conducted Mott-Schottky tests to make qualitative analysis of these two passive structures (Supplementary Note 2). Despite the morphologic difference, they exhibit virtually identical semiconductor features (Supplementary Fig. 5). Additionally, by estimating the slope of

https://doi.org/10.1038/s41467-025-64875-0

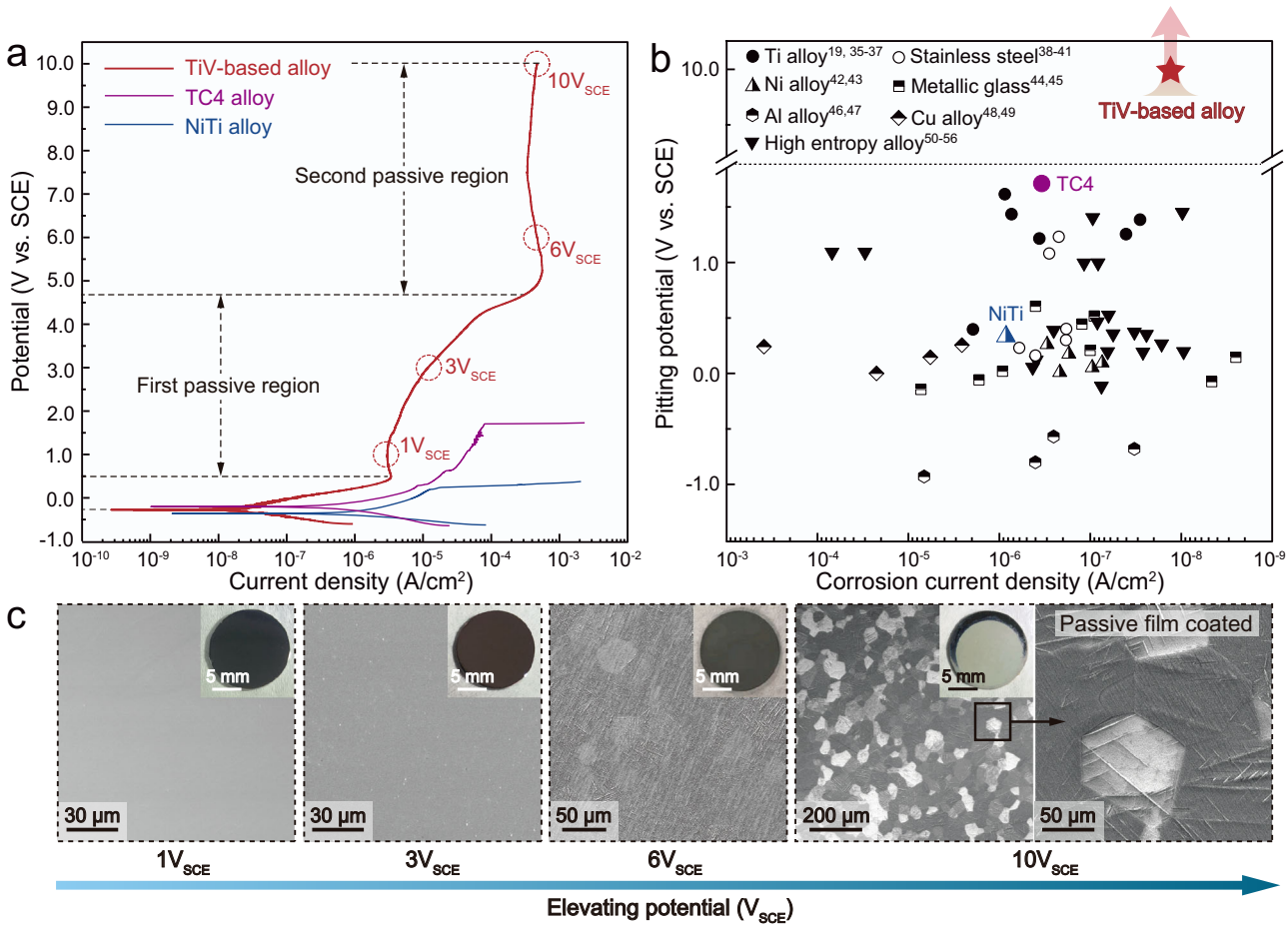

Fig. 2 | Electrochemical performance of the TiV-based alloy. a Potentiodynamic polarization curve of the TiV-based alloy. Polarization curves of the commercial TC4 and NiTi alloys are also plotted for direct comparison. **b** Comparison of the present TiV-based alloy against other conventional alloys in terms of their i_{corr} versus E_{pit} in 3.5 wt.% NaCl solution. These alloys include Ti alloys[19,35–37], stainless steels[38–41], Ni alloys[42,43], metallic glasses[44,45], Al alloy[46,47], Cu alloy[48,49], and high entropy alloys[50–56]. **c** Scanning electron microscope (SEM) images and macro photographs showing the evolution of the passivated surface with increasing anodic potential. Source data for (**a** and **b**) are provided as a Source data file.

linear portions in the n-type and p-type semiconductor responses, the layer-structured passive barrier is generally found to have lower donor and acceptor densities, indicating its fewer point defects and better capability to withstand extreme anodic potentials[62]. From an in-depth microstructural perspective, the passive layers at 6 V_{SCE} display a mixture of amorphous and nanocrystalline structures, in contrast to the amorphous structure at 3 V_{SCE} (Supplementary Fig. 6). This indicates that higher anodic potentials accelerate the kinetics of structural ordering, resulting in a different passivation process involving localized crystallization and the appearance of a second passive region. This crystalline character has been reported to enhance the protectiveness of passive films[63,64].

It is well-known that the chemical composition and elemental valence state of the passive film are closely related to the corrosion resistance of alloys. Therefore, the passive film properties of the TiV-based alloy were characterized using X-ray photoelectron spectroscopy (XPS), as shown in Fig. 4. To reveal the origin of its superb corrosion resistance, a passivated NiTi alloy was also prepared for direct comparison. The TiV-based and NiTi specimens were potentiostatically polarized in the passive region at 0.8 V_{SCE} and 0 V_{SCE}, respectively, which were slightly higher than their respective E_{corr} (Fig. 2a). Figure 4a shows the potentiostatic polarization curves of the alloys. The current densities of the two alloys exhibit no significant difference, decreasing to below 5×10^{-7} A/cm^2 by the end of the polarization to form a stable passive film on the alloy surface. Figure 4b shows the XPS spectrum of the TiV-based alloy, giving detailed information on peak positions and the proportion of valence states for individual elements. The fitting results show that the O *1s* spectrum decomposes to O^{2-} in oxide species and OH^- in hydroxides, which account for 87.3% and 12.7% of the O *1s* peak intensity, respectively. Other elements primarily exist as metallic oxides, which have beneficial effects on corrosion resistance. The cationic composition of the passive film, summarized in the bar graph at the bottom of Fig. 4b, indicates that TiO_2, V_{ox}^{3+}/ V_{ox}^{5+} oxides, and Al_2O_3 collectively make up nearly 99% of the film. These findings are further supported by the formation energy of metallic oxides calculated in Supplementary Fig. 7, where Al_2O_3 and V_{ox}^{3+}/ V_{ox}^{5+} oxides have the lowest Gibbs free energy, and TiO_2 contributes as the primary component due to the dominant titanium content. Consequently, the passive film, with a thickness of ~10 nm, is oxygen-enriched and shows a detectable distribution of Ti, V, and Al, confirmed by the HRTEM and EDS scanning in Supplementary Fig. 8. In strong contrast, the XPS results of the NiTi alloy in Fig. 4c reveal a significantly higher proportion of OH^- in the O *1s* spectrum, reaching 48.5%. This excessive OH^- is linked to the formation of Ni hydroxide, accounting for 23.48% in the Ni *2p* spectrum. No metallic hydroxide, on the other hand, is identified in the TiV-based alloy. High concentrations of metallic hydroxides are known to destabilize the passive film and reduce corrosion resistance[62,65,66]. The absence of metallic hydroxide in the Ti-V alloy, therefore, contributes to its superb electrochemical stability. Additionally, metallic states,

such as V^0 and Ti^0, are identified in the passive film of both alloys. These metallic states are typically derived from the alloy substrate, suggesting an ultrathin passive film or lower O content beneath the passive surface[67,68].

Resistance to SCC

The mechanical reliability of the TiV-based alloy in 3.5 wt.% NaCl solution was investigated by slow strain-rate tensile (SSRT) experiments, as shown in Fig. 5. The SSRT tests in air were also conducted to elucidate the influence of the aggressive environment. It can be seen that the mechanical properties, including the critical stress for the double yielding and the ultimate tensile strength (UTS), exhibit no significant difference between the two environments (Fig. 5a). Notably, alloys in both environments retained the same UTS of ~860 MPa, strengthened by the stress-induced martensitic transformation from β to α'' and precipitation strengthening from the ω phase. Meanwhile, the total elongation (TE) of the alloy decreased by only ~2.3% in 3.5 wt.% NaCl solution, from ~29.2% to ~26.9%. The SCC specimen exhibits a ductile fracture mode, as evidenced by the fracture surface containing abundant and uniform dimples (inset of Fig. 5a). By maintaining the high strength along with a minimal loss of ductility, the alloy demonstrates superior resistance to SCC compared to other commercial alloys for marine applications, including the standard TC4 and TC4 ELI alloys commonly employed in shipbuilding industries (Supplementary Table 2). When examining the sample surfaces, typical microcracks due to SCC are found distributing occasionally on the gauge surface (Fig. 5b, c), whereas the tensile specimen tested in air shows no presence of developed microcracks (Supplementary Fig. 9). The cross-sectional analysis indicates that the maximum crack depth on the gauge surface is ~12 μm (Fig. 5d), significantly less than the thickness of the SCC specimens. The results suggest that the microcracks have a very limited effect on the alloy's ductility due to their constrained propagation.

It is well-documented that SCC behaves in a hierarchical manner of crack initiation, growth, and propagation[69,70]. Cracks generally initiate at sites with surface or chemical discontinuities, such as corrosion pits, grain boundaries, and slip bands[71–75]. Guaranteed by the superb electrochemical stability and chemical homogeneity of the TiV-based alloy, potential crack-nucleating sites, such as the corrosion pits and grain-boundary corrosion, were inhibited (Fig. 2). Instead, transgranular SCC initiated at the slip bands, where the emergence of slip steps disrupted the passive film, exposing the fresh and reactive substrate material for crack initiation (Fig. 5c). In such a case associated

Table 1 | Electrochemical parameters of the TiV-based, TC4, and NiTi alloys

Alloys	E_{corr} (V_{SCE})	i_{corr} (nA/cm²)	E_{pit} (V_{SCE})
TiV-based alloy	−0.263	13.9	>10
TC4 alloy	−0.206	417.7	1.685
NiTi alloy	−0.354	574.5	0.245

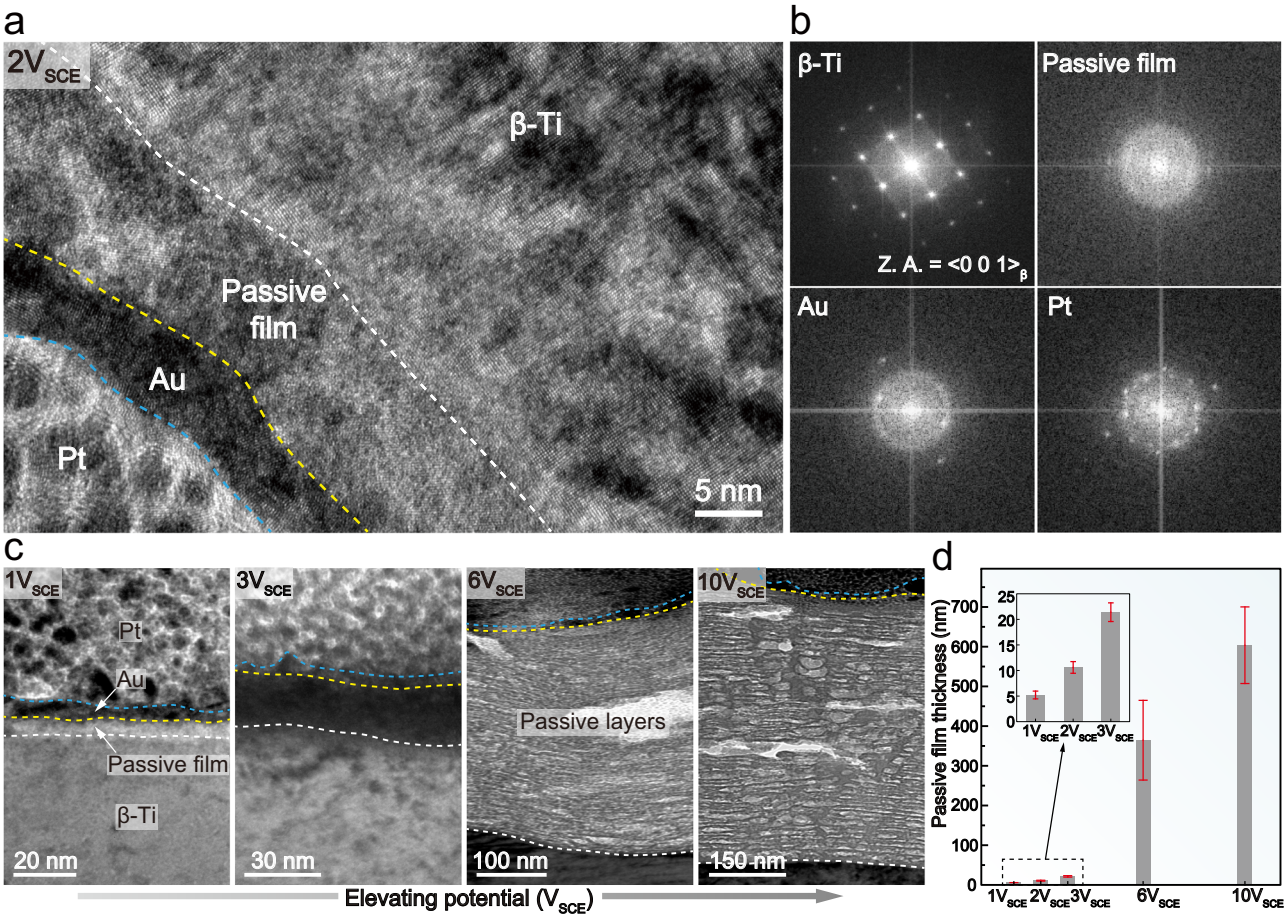

Fig. 3 | Evolution of the passive film during potentiodynamic polarization. **a** HRTEM image of the passive film polarized to 2 V_{SCE}. **b** FFT patterns of different layers marked in (**a**). **c** TEM BF images showing the thickening of passive films with increasing potentials. **d** The evolution of passive film thickness during potentiodynamic polarization. The error bars represent the standard deviation of the statistical measurement of passive film thickness. The measurement of passive film thickness was derived from three independent samples, each measured at 5 different locations. Source data for (**d**) are provided as a Source data file.

https://doi.org/10.1038/s41467-025-64875-0

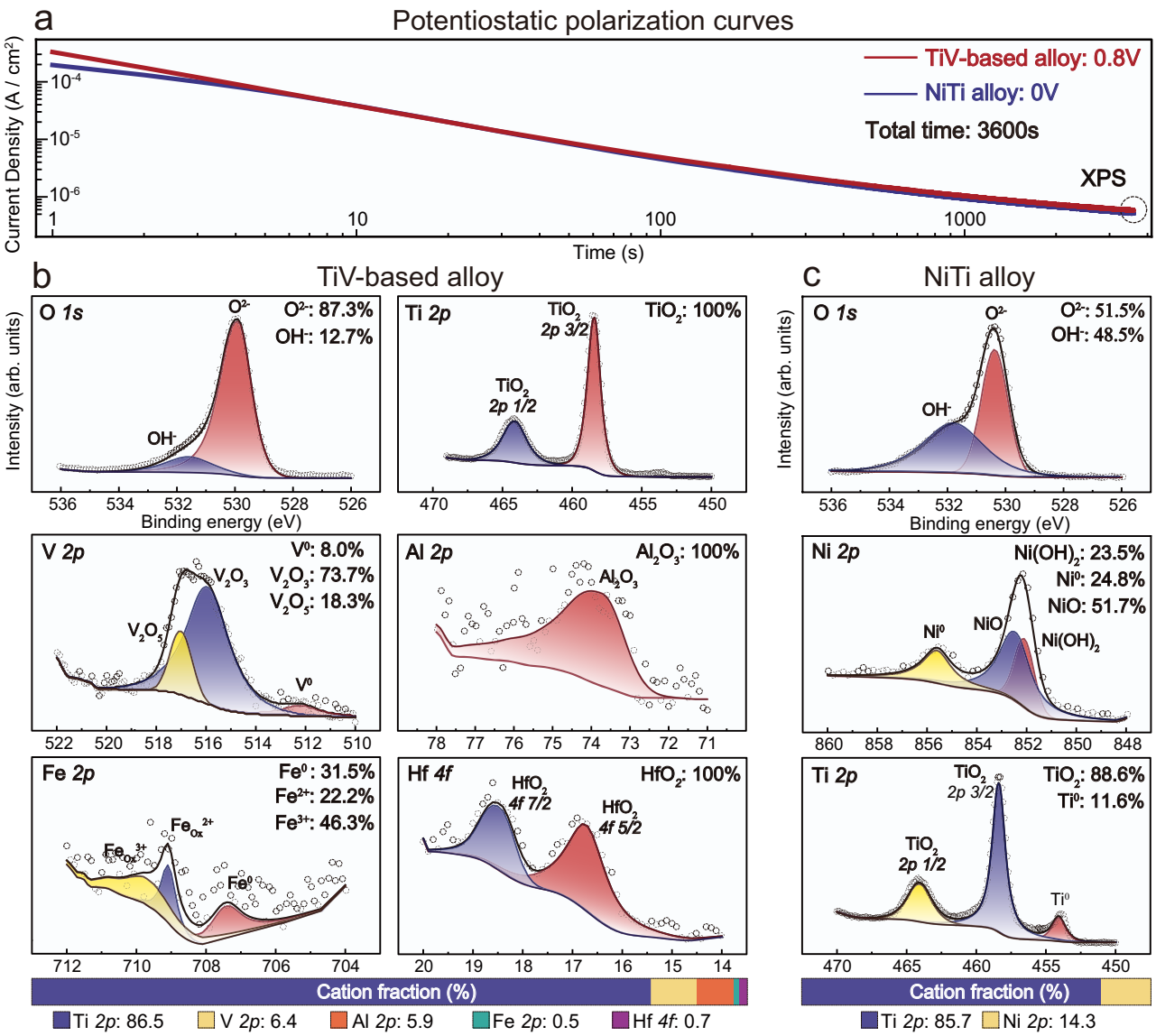

Fig. 4 | XPS analysis of the TiV-based and NiTi alloys. a Potentiostatic polarization curves. **b**, **c** High-resolution spectra of the TiV-based and NiTi alloys, respectively. The cationic proportion of the passive film is summarized in the bar graph at the bottom of the figure. Source data are provided as a Source data file.

with the micro-cleavages, a typical film-induced cleavage model is generally used to describe the propagation of transgranular SCC[29,72,73,76]. This model suggests that when a crack nucleates and attains a velocity to advance toward the underlying substrate, it becomes progressively blunted by plastic deformation, and the passive film re-establishes on the crack tip. The repaired passive film can resist the anodic dissolution of the alloy matrix until the next stress-induced rupture. The crack propagation is then progressed by repeating this rupture-repair cycle, meaning that the regeneration of a stable passive film before the occurrence of the next cleavage is crucial to resist the anodic dissolution and slow down the crack propagation[29]. Figure 5e shows a microcrack of ~4.2 μm in depth, beneath the passive film ruptured by a slip step. Evidently, an oxide layer can be found covering the crack tip and its neighboring area (Fig. 5f, g), indicating that the exposed metal upon film rupture can be repassivated in a short time. As a result, the crack propagation was greatly constrained, and an excellent damage tolerance of SCC was thereby achieved in this titanium alloy.

In summary, we successfully developed a damage-tolerant titanium alloy with exceptional corrosion resistance in an aggressive saline solution. Our work demonstrated an unprecedented pitting resistance in the TiV-based alloy but also addressed the gap in fundamentally understanding the passive behavior of alloys under extreme corrosion conditions. A chemistry-microstructure-property relationship was established for the comprehensive understanding of its corrosion resistance. The alloy's excellent electrochemical stability stems from its resilient passivation in different passive regions. The compact nature of passive film, as well as reduced OH^- concentration, all contribute to its electrochemical stability. Supported by this superb electrochemical stability, excellent mechanical reliability was also achieved due to the fast repair of the passive film and the prevention of localized corrosion that could lead to crack nucleation. It is expected that such exceptional electrochemical and mechanical stability would enhance the prosperous perspective of titanium alloys in marine applications.

Methods

Materials fabrication

Ingot with the nominal composition of $Ti_{82.19}V_{12.5}Al_{3.5}Fe_{0.8}Hf_1B_{0.01}$ (at. %) was fabricated using the non-consumable arc melting under a

https://doi.org/10.1038/s41467-025-64875-0

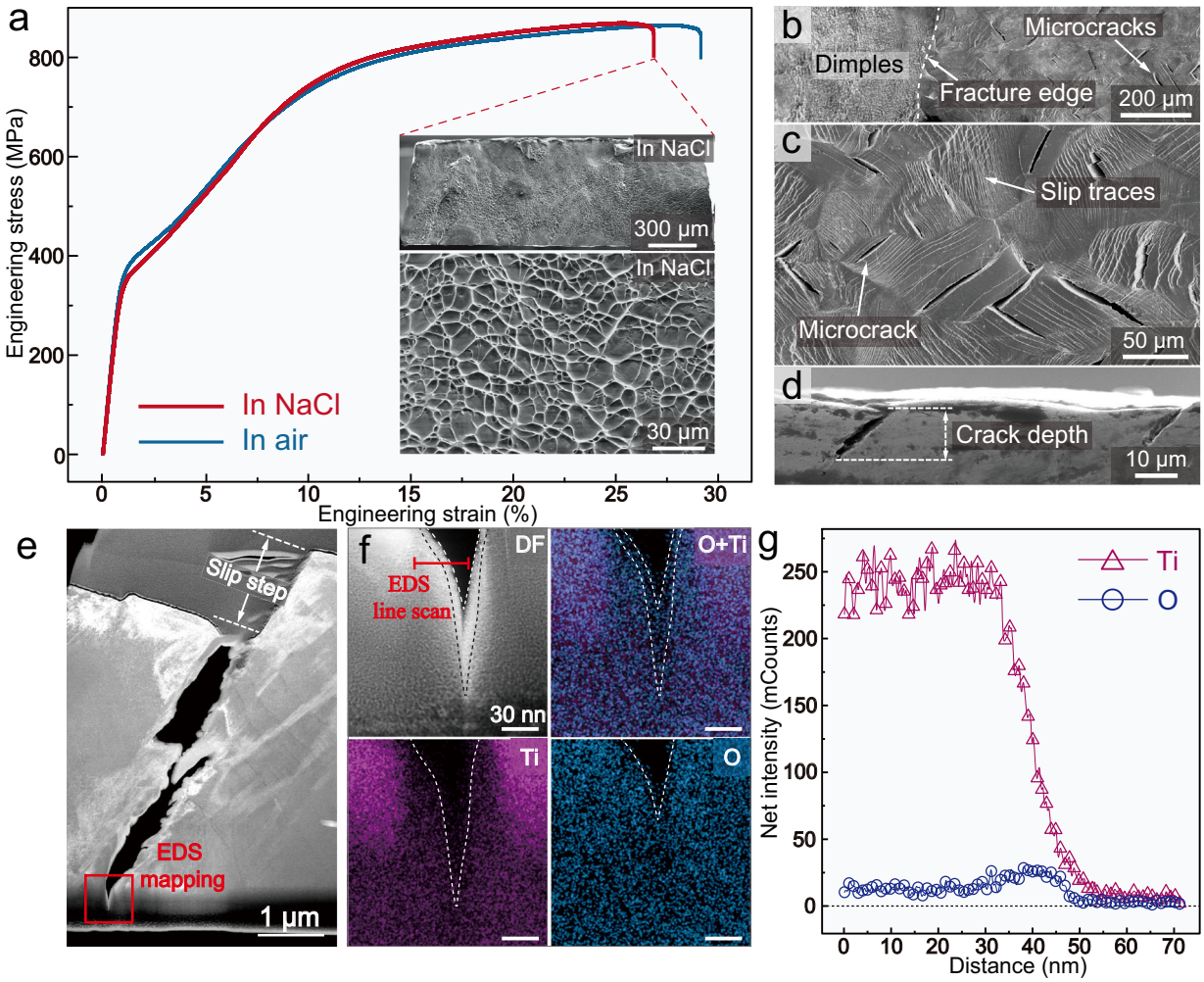

Fig. 5 | SCC of the TiV-based alloy. a Engineering stress-strain curves of SSRT tests conducted in 3.5 wt.% NaCl solution and air, respectively. The two inset images display the fracture surface at low and high magnifications after the SSRT test in NaCl solution. **b, c** SEM images presenting the microcracks on the gauge surface. **d** Cross-section view of the gauge section. **e** TEM images showing the cross-sectional microstructure of a microcrack. **f** EDS mapping of the crack tip area marked by the solid-line square in (**e**). **g** The left-to-right EDS line scan near the crack tip area marked in (**f**), showing detectable oxygen enrichment on the alloy matrix. Source data for (**a** and **g**) are provided as a Source data file.

pure argon atmosphere. The sample was melted five times to ensure chemical homogeneity and then drop casted into a water-cooled copper mold with a cross section of 5 mm × 12 mm. The as-cast ingot then experienced several multi-step cold rollings to reach the thickness of 3.5, 2.2, and 1.2 mm. Each interval was followed by an intermediate annealing at 900 °C for 3600 s and water quenching. Thereafter, the grain size of the samples was further refined through thermal-mechanical training. Specifically, the alloy was continually cold rolled to the thickness of 1.1, 1.0, 0.9, and 0.8 mm. A short-time intermediate annealing at 1100 °C for 15 s was performed at each interval, followed by water quenching. Theoretical density (D) of the alloy was calculated by the following formula $D = 100 / (\sum c_x / d_x)$, where c_x and d_x represent the weight percent and density of element x, respectively[77].

Microstructural characterization

The XRD (D2 PHASE XE-T) operating with a Cu Kα X-ray source was conducted to identify the phase constituent. The characterization of the initial structure was performed by EBSD using an EDAX detector equipped in the SEM (FEI scios). The EBSD results were analyzed using the EDAX OIM Analysis 8 software. Samples for EBSD characterization were firstly mechanically polished to mirror-bright, and then electro-polished in a solution of HNO_3: CH_3OH (1:4) at a cryogenic temperature below − 40 °C. The nanoscale microstructure was further investigated using TEM (JEM-2100F). The TEM specimen was mechanically ground and then punched to a disk of Φ3 mm for the final thinning process by the PIPS II PRO precision ion-milling system. The characterization of the passive film included planar and cross-sectional analysis. The planar observation of the passive film was directly performed by SEM. For the cross-sectional characterization, TEM specimens were lifted out by the focused ion beam (FIB) using a Ga^+ source. Before FIB processing, a thin layer of Au was pre-deposited on the top of passive films by a vacuum-sputtering equipment (Smart Coater, JEOL) to avoid damage to the passive surface. For the measurement of passive film thickness, TEM specimens were lifted out from random grains for microstructural observation. Compositional analysis of the cross-sectional passive film was performed using a scanning transmission electron microscopy (STEM, Talos F200X, FEI) equipped with a Super-X EDS detector.

Chemical information of the surface films, which were pre-grown in 3.5 wt.% NaCl solution for 3600 s by potentiostatic polarization at the onset of passive regions, was analyzed using XPS (Escalab Xi+, thermo scientific) with an Al Kα radiation (1486.6 eV). During XPS, high-resolution spectra of C *1s*, O *1s*, Ti *2p*, V *2p*, Al *2p*, Fe *2p*, and Hf *4f* were obtained at a pass energy of 20 eV with an energy step of 0.1 eV. The XPS measurements were

performed on three random areas for each specimen to ensure data validity. For comparison, the XPS specimens of the NiTi alloy were also prepared. The XPS spectra were analyzed using the Avantage software. The binding energies of all elements were first calibrated according to the adventitious C *1s* signal at 284.8 eV, and then background subtracted by the Shirley-type algorithm. Subsequently, the individual spectrum was fitted based on the Gaussian-Lorentzian product function and the known binding energies of various elemental valence states.

Electrochemical tests

Corrosion resistance was evaluated by the conventional polarization method[78]. Specimens with a diameter of 14 mm were cut from the alloy sheets using the water-jet cutting machine and then mechanically polished to a mirror-bright finish. Electrochemical experiments were performed in a conventional three-electrode system connected to the electrochemical workstation (CHI 760E) at room temperature. In this setup, the specimen served as the working electrode, a thin platinum plate as the counter electrode, and a saturated calomel electrode (SCE) as the reference electrode. A rubber O-ring was placed around and pressed on the working electrode to an exposed area of 1 cm^2. The electrolyte used for electrochemical tests was 3.5 wt.% NaCl. Before testing, the working electrode was cathodically polarized at −0.8 V_{SCE} for 300 s to minimize the air-oxidation effect, followed by stabilization at OCP for 3600 s. The EIS measurements were performed in a frequency range from 10^5 Hz to 10^{-2} Hz with a sinusoidal voltage amplitude of 10 mV. The potentiodynamic polarization test involved anodically polarizing the working electrode from −0.6 V_{SCE} to various potentials at a scan rate of 1 mV/s[79]. At least three specimens were tested for the EIS measurements and the potentiodynamic polarization experiments. The same EIS measurements and potentiodynamic polarization tests for the commercial TC4 and NiTi alloys were also conducted to elucidate the electrochemical performance of the TiV-based alloy. Semiconductor characteristics of the passive film were determined by the Mott-Schottky test, by measuring the passive surface using an alternating current voltage with an amplitude of ± 10 mV and a fixed frequency of 1 kHz with a step of 20 mV from −1.0 V_{SCE} to 1.0 V_{SCE}.

SCC tests

The SCC resistance was evaluated by the typical SSRT tests[72]. Tensile specimens with the gauge dimension of 3.5 mm × 0.8 mm × 12.5 mm were cut from the Ti-V alloy sheet using the water-jet cutting machine. The SSRT experiments were conducted by uniaxial tensile tests in 3.5 wt. % NaCl solution at room temperature with a strain rate of 10^{-6}/s. The specimen surface was mechanically ground with 5000-grit SiC abrasive paper before testing. After fracture, specimens were removed from the NaCl solution within 5 minutes to prevent further passivation of the microcracks. The SSRT tests in air were also performed to assess the susceptibility to SCC. At least three specimens were tested for each environment. The loss of UTS (FE_{loss}) and TE (EL_{loss}), as well as the SCC susceptibility index (I_{SSRT}), are calculated using the following equations:

$$FE_{loss} = 1 - \frac{\sigma_{NaCl}}{\sigma_{air}} \quad (1)$$

$$EL_{loss} = 1 - \frac{\varepsilon_{NaCl}}{\varepsilon_{air}} \quad (2)$$

$$I_{SSRT} = 1 - \frac{\sigma_{NaCl}(1+\varepsilon_{NaCl})}{\sigma_{air}(1+\varepsilon_{air})} \quad (3)$$

where σ_{NaCl} and σ_{air} are the UTS in 3.5 wt.% NaCl solution and air, respectively, and ε_{NaCl} and ε_{air} are the respective TE.

Data availability

All source data for these findings are provided as a Source Data file and via Figshare[80]. Source data are provided with this paper.

References

1. Devaraj, A. et al. A low-cost hierarchical nanostructured beta-titanium alloy with high strength. *Nat. Commun.* **7**, 11176 (2016).
2. Zhu, Q. et al. Towards development of a high-strength stainless Mg alloy with Al-assisted growth of passive film. *Nat. Commun.* **13**, 5838 (2022).
3. Wang, Z. et al. Nature-Inspired Incorporation of Precipitants into High-Strength Bulk Aluminum Alloys Enables Life-Long Extraordinary Corrosion Resistance in Diverse Aqueous Environments. *Adv. Mater.* **36**, 2406506 (2024).
4. Spece, H. et al. A systematic review of preclinical in vivo testing of 3D printed porous Ti6Al4V for orthopedic applications, part I: Animal models and bone ingrowth outcome measures. *J. Biomed. Mater. Res. B Appl. Biomater.* **109**, 1436–1454 (2021).
5. Schumacher, M. M. et al. Seawater corrosion handbook. (Noyes Data Corporation, New Jersey, 1979).
6. Bardal, E., Drugli, J. M. & Gartland, P. O. The behaviour of corrosion-resistant steels in seawater: a review. *Corros. Sci.* **35**, 257–267 (1993).
7. Yang, J., Song, Y., Dong, K. & Han, E. H. Research progress on the corrosion behavior of titanium alloys. *Corros. Rev.* **41**, 5–20 (2023).
8. Kaminaka, H., Abe, M., Matsumoto, S., Kimura, K. & Kamio, H. Characteristics and applications of high corrosion resistant titanium alloys. *Nippon Steel Sumitomo Met. Tech. Rep.* **106**, 34–40 (2014).
9. Yan, S. et al. state-of-the-art review on passivation and biofouling of Ti and its alloys in marine environments. *J. Mater. Sci. Technol.* **34**, 421–435 (2018).
10. Gorynin, I. V. Titanium alloys for marine application. *Mater. Sci. Eng. A* **263**, 112–116 (1999).
11. Kapranos, P. & Priestner, R. Overview of metallic materials for heat exchangers for ocean thermal energy conversion systems. *J. Mater. Sci.* **22**, 1141–1149 (1987).
12. Mountford Jr, J. A. et al. Titanium-properties, advantages and applications solving the corrosion problems in marine service. *Proc. CORROSION 2002*. Denver, CO. Paper No: C2002-02170, pp. 1–28 (2002).
13. Jani, J. M., Leary, M., Subic, A. & Gibson, M. A. A review of shape memory alloy research, applications and opportunities. *Mater. Des.* **56**, 1078–1113 (2015). 1980-.
14. Angilella, A. J., Gandhi, F. S. & Miller, T. F. Design and testing of a shape memory alloy buoyancy engine for unmanned underwater vehicles. *Smart Mater. Struct.* **24**, 115018 (2015).
15. Shokri, A. & Fard, M. S. Corrosion in seawater desalination industry: a critical analysis of impacts and mitigation strategies. *Chemosphere* **307**, 135640 (2022).
16. Prando, D. et al. Corrosion of titanium: Part 1: Aggressive environments and main forms of degradation. *J. Appl. Biomater. Funct. Mater.* **15**, e291–e302 (2017).
17. Mahoney, M. W. & Tetelman, A. S. The effect of microstructure on the hot salt stress corrosion susceptibility of titanium alloys. *Metall. Trans. A* **7**, 1549–1558 (1976).
18. Brossia, C. S. & Cragnolino, G. A. Effect of palladium on the corrosion behavior of titanium. *Corros. Sci.* **46**, 1693–1711 (2004).
19. Dai, N., Zhang, L. C., Zhang, J., Chen, Q. & Wu, M. Corrosion behavior of selective laser melted Ti-6Al-4 V alloy in NaCl solution. *Corros. Sci.* **102**, 484–489 (2016).
20. Cui, Y. W. et al. Metastable pitting corrosion behavior of laser powder bed fusion produced Ti-6Al-4V in Hank's solution. *Corros. Sci.* **203**, 110333 (2022).
21. Chen, Y. H. et al. In-vitro and in-vivo bio-corrosion and biocompatibility responses of bioactive TiTaNb films with various Ta contents on Ti6Al4V implants. *J. Mater. Res. Technol.* **25**, 3803–3818 (2023).

22. Cheng, Y., Cai, W. & Zhao, L. C. Effects of Cl− ion concentration and pH on the corrosion properties of NiTi alloy in NaCl solution. *J. Mater. Sci.* **22**, 239–240 (2003).
23. Frankel, G. S. Pitting corrosion of metals: a review of the critical factors. *J. Electrochem. Soc.* **145**, 2186 (1998).
24. Lu, J. et al. Effect of microstructure characteristic on mechanical properties and corrosion behavior of new high strength Ti–1300 beta titanium alloy. *J. Alloy. Compd.* **727**, 1126–1135 (2017).
25. Varshney, P. & Kumar, N. Stress Corrosion Cracking Study of Fe39Mn20Co20Cr15Si5Al1 (at.%) compositionally complex alloy in 3.5 wt% NaCl salt solution. *TMS 2022 151st Annual Meeting & Exhibition Supplemental Proceedings* 1138–1145 (2022).
26. Kolkman, H. J., Kool, G. A. & Wanhill, R. J. H. Aircraft crash caused by stress corrosion cracking. *J. Eng. Gas. Turbine Power* **118**, 146–149 (1996).
27. Luo, S. et al. Stress corrosion cracking behavior and mechanism of super 13Cr stainless steel in simulated O2/CO2 containing 3.5 wt% NaCl solution. *Eng. Fail. Anal.* **130**, 105748 (2021).
28. Khalissi, M., Raman, R. K. S. & Khoddam, S. Stress corrosion cracking of novel steel for automotive applications. *Procedia Eng.* **10**, 3381–3386 (2011).
29. Dong, Y. et al. Stress corrosion cracking of TC4 ELI alloy with different microstructure in 3.5% NaCl solution. *Mater. Charact.* **194**, 112357 (2022).
30. Kang, S. et al. Effect of chloride ion concentration on stress corrosion cracking and electrochemical corrosion of high manganese steel. *High. Temp. Mater. Process* **41**, 389–402 (2022).
31. Ding, Y. et al. Effects of microstructure on the stress corrosion cracking behavior of nickel-aluminum bronze alloy in 3.5% NaCl solution. *Mater. Sci. Eng. A* **733**, 361–373 (2018).
32. Yang, Y. et al. Corrosion and passivation of annealed Ti–20Zr–6.5 Al–4V alloy. *Corros. Sci.* **101**, 56–65 (2015).
33. Stern, M. & Geary, A. L. Electrochemical polarization: I. a theoretical analysis of the shape of polarization curves. *J. Electrochem. Soc.* **104**, 56 (1957).
34. Burstein, G. T., Liu, C., Souto, R. M. & Vines, S. P. Origins of pitting corrosion. *Corros. Eng. Sci. Technol.* **39**, 25–30 (2004).
35. Zhang, H. et al. Influence of phase composition on stress-corrosion cracking of Ti-6Mo-5V-3Al-2Fe-2Zr alloy in 3.5% NaCl solution. *Crystals* **12**, 1794 (2022).
36. Luo, S., Yan, P., Liu, M., Xue, Y. & Song, W. Electrochemical corrosion behavior of TA2 titanium alloy welded joint in Cl-containing solutions. *Int. J. Electrochem. Sci.* **16**, 21096 (2021).
37. Delgado-Alvarado, C. & Sundaram, P. A. A study of the corrosion behavior of gamma titanium aluminide in 3.5 wt% NaCl solution and seawater. *Corros. Sci.* **49**, 3732–3741 (2007).
38. Yi, J. Z., Hu, H. X., Wang, Z. B. & Zheng, Y. G. Comparison of critical flow velocity for erosion-corrosion of six stainless steels in 3.5 wt% NaCl solution containing 2 wt% silica sand particles. *Wear* **416**, 62–71 (2018).
39. Fu, A. et al. A novel supersaturated medium entropy alloy with superior tensile properties and corrosion resistance. *Scr. Mater.* **186**, 381–386 (2020).
40. Hsu, Y. J., Chiang, W. C. & Wu, J. K. Corrosion behavior of FeCoNiCrCux high-entropy alloys in 3.5% sodium chloride solution. *Mater. Chem. Phys.* **92**, 112–117 (2005).
41. Fu, J. et al. Effect of Nb addition on the microstructure and corrosion resistance of ferritic stainless steel. *Appl. Phys. A* **126**, 194 (2020).
42. Ming, T., Peng, Q., Han, Y. & Zhang, T. Effect of water jet cavitation peening on electrochemical corrosion behavior of nickel-based alloy 600 in NaCl solution. *Mater. Chem. Phys.* **295**, 127122 (2023).
43. Liu, L., Li, Y. & Wang, F. Influence of micro-structure on corrosion behavior of a Ni-based superalloy in 3.5% NaCl. *Electrochim. Acta* **52**, 7193–7202 (2007).
44. Gu, J., Shao, Y., Shi, L., Si, J. & Yao, K. Novel corrosion behaviours of the annealing and cryogenic thermal cycling treated Ti-based metallic glasses. *Intermetallics* **110**, 106467 (2019).
45. Gong, P. et al. Corrosion behavior of TiZrHfBeCu (Ni) high-entropy bulk metallic glasses in 3.5 wt.% NaCl. *npj mater. degrad.* **6**, 77 (2022).
46. Ezuber, H., El-Houd, A. & El-Shawesh, F. A study on the corrosion behavior of aluminum alloys in seawater. *Mater. Des.* **29**, 801–805 (2008).
47. Zhang, K. et al. Inhibitory effect of konjac glucomanan on pitting corrosion of AA5052 aluminium alloy in NaCl solution. *J. Colloid Interface Sci.* **517**, 52–60 (2018).
48. Tsao, L. C. & Chen, C. W. Corrosion characterization of Cu–Sn intermetallics in 3.5 wt.% NaCl solution. *Corros. Sci.* **63**, 393–398 (2012).
49. Xia, T. et al. Enhanced corrosion resistance of a Cu10Ni alloy in a 3.5 wt% NaCl solution by means of ultrasonic surface rolling treatment. *Surf. Coat. Tech.* **363**, 390–399 (2019).
50. Raza, A., Abdulahad, S., Kang, B., Ryu, H. J. & Hong, S. H. Corrosion resistance of weight reduced AlxCrFeMoV high entropy alloys. *Appl. Surf. Sci.* **485**, 368–374 (2019).
51. Chou, Y. L., Yeh, J. W. & Shih, H. C. The effect of molybdenum on the corrosion behaviour of the high-entropy alloys Co1. 5CrFeNi1. 5Ti0. 5Mox in aqueous environments. *Corros. Sci.* **52**, 2571–2581 (2010).
52. Shi, Y. et al. Homogenization of AlxCoCrFeNi high-entropy alloys with improved corrosion resistance. *Corros. Sci.* **133**, 120–131 (2018).
53. Li, J., Yang, X., Zhu, R. & Zhang, Y. Corrosion and serration behaviors of TiZr0. 5NbCr0. 5V x Mo y high entropy alloys in aqueous environments. *Metals* **4**, 597–608 (2014).
54. Shi, Y. et al. Corrosion of Al xCoCrFeNi high-entropy alloys: Al-content and potential scan-rate dependent pitting behavior. *Corros. Sci.* **119**, 33–45 (2017).
55. Lu, C. W., Lu, Y. S., Lai, Z. H., Yen, H. W. & Lee, Y. L. Comparative corrosion behavior of Fe50Mn30Co10Cr10 dual-phase high-entropy alloy and CoCrFeMnNi high-entropy alloy in 3.5 wt% NaCl solution. *J. Alloy. Compd.* **842**, 155824 (2020).
56. Zhao, Y. et al. Effects of Ti-to-Al ratios on the phases, microstructures, mechanical properties, and corrosion resistance of Al2-xCoCrFeNiTix high-entropy alloys. *J. Alloy. Compd.* **805**, 585–596 (2019).
57. González, J. E. G. & Mirza-Rosca, J. C. Study of the corrosion behavior of titanium and some of its alloys for biomedical and dental implant applications. *J. Electroanal. Chem.* **471**, 109–115 (1999).
58. Socorro-Perdomo, P. P., Florido-Suárez, N. R., Mirza-Rosca, J. C. & Saceleanu, M. V. EIS characterization of Ti alloys in relation to alloying additions of Ta. *Materials* **15**, 476 (2022).
59. de Assis, S. L., Wolynec, S. & Costa, I. Corrosion characterization of titanium alloys by electrochemical techniques. *Electrochim. Acta* **51**, 1815–1819 (2006).
60. Figueira, N., Silva, T. M., Carmezim, M. J. & Fernandes, J. C. S. Corrosion behaviour of NiTi alloy. *Electrochim. Acta* **54**, 921–926 (2009).
61. Hamada, E. et al. Direct imaging of native passive film on stainless steel by aberration corrected STEM. *Corros. Sci.* **52**, 3851–3854 (2010).
62. Luo, H. et al. A strong and ductile medium-entropy alloy resists hydrogen embrittlement and corrosion. *Nat. Commun.* **11**, 3081 (2020).

63. Gai, X. et al. Electrochemical behaviour of passive film formed on the surface of Ti-6Al-4V alloys fabricated by electron beam melting. *Corros. Sci.* **145**, 80–89 (2018).
64. Li, D. G., Wang, J. D., Chen, D. R. & Liang, P. Influence of passive potential on the electronic property of the passive film formed on Ti in 0.1 M HCl solution during ultrasonic cavitation. *Ultrason. Sonochem.* **29**, 48–54 (2018).
65. Clayton, C. R. & Lu, Y. C. A bipolar model of the passivity of stainless steel: the role of Mo addition. *J. Electrochem. Soc.* **133**, 2465 (1986).
66. Zhang, J. Y. et al. The influence of microstructural evolutions on electrochemical corrosion and passive behavior in precipitation-strengthened high-entropy alloys. *Corros. Sci.* **233**, 112074 (2024).
67. Zhao, H. et al. How solute atoms control aqueous corrosion of Al-alloys. *Nat. Commun.* **15**, 561 (2024).
68. Carmezim, M. J., Simoes, A. M., Montemor, M. F. & Belo, M. D. C. Capacitance behaviour of passive films on ferritic and austenitic stainless steel. *Corros. Sci.* **47**, 581–591 (2005).
69. Fujii, T., Hisada, Y., Tohgo, K. & Shimamura, Y. Investigation on nucleation of intergranular stress corrosion cracking in austenitic stainless steel by in situ strain measurement. *Mater. Sci. Eng. A* **773**, 138858 (2020).
70. Tohgo, K., Suzuki, H., Shimamura, Y., Nakayama, G. & Hirano, T. Monte Carlo simulation of stress corrosion cracking on a smooth surface of sensitized stainless steel type 304. *Corros. Sci.* **51**, 2208–2217 (2009).
71. Fujii, T., Tohgo, K., Kenmochi, A. & Shimamura, Y. Experimental and numerical investigation of stress corrosion cracking of sensitized type 304 stainless steel under high-temperature and high-purity water. *Corros. Sci.* **97**, 139–149 (2015).
72. Jones, R. H. Stress-corrosion cracking, corrosion: fundamentals, testing, and protection. *ASM Int.* **13A**, 346–366 (2003).
73. Meletis, E. I. A review of present mechanisms of transgranular stress corrosion cracking. *J. Mech. Behav. Mater.* **7**, 1–14 (1996).
74. Parkins, R. N. Localized corrosion and crack initiation. *Mater. Sci. Eng. A* **103**, 143–156 (1988).
75. Elboujdaini, M. et al. Stress corrosion crack initiation processes: pitting and microcrack coalescence. *CORROSION 2000. Association for Materials Protection and Performance*, 1–31 (2000).
76. Sieradzki, K. & Newman, R. C. Brittle behavior of ductile metals during stress-corrosion cracking. *Philos. Mag. A* **51**, 95–132 (1985).
77. Ogawa, Y., Ando, D., Sutou, Y. & Koike, J. A lightweight shape-memory magnesium alloy. *Science* **353**, 368–370 (2016).
78. Mansfeld, F., Liu, G., Xiao, H., Tsai, C. H. & Little, B. J. The corrosion behavior of copper alloys, stainless steels and titanium in seawater. *Corros. Sci.* **36**, 2063–2095 (1994).
79. American Society for Testing and Materials. ASTM G5-14, Standard reference test method for making potentiodynamic anodic polarization measurements. *ASTM* (ASTM International, West Conshohocken, PA, USA, 2014).
80. Zhang, J. X. et al. Achieving electrochemical and mechanical stability in a lightweight titanium alloy. Figshare https://doi.org/10.6084/m9.figshare.29651018 (2025).

Acknowledgements

The authors greatly acknowledge the financial support from the Hong Kong Research Grant Council (RGC) (Grant No. C1020-21G) and the City University of Hong Kong (Grant No. 9229121).

Author contributions

T.Y., J.X.Z., and J.Y.Z. conceptualized the project and designed the research; J.X.Z. fabricated the samples; J.Y.Z., X.E.L. and X.L. performed the electrochemical tests; J.X.Z. and J.Y.Z. conducted the SCC test; J.X.Z. conducted the EBSD and SEM tests; J.X.Z. and W.C.X. performed the TEM-sample preparation and characterization; J.X.Z., J.Y.Z., and N.L. analyzed the data and wrote the manuscript; J.X.Z., J.Y.Z., H.L., and P.K.L. revised the manuscript; All authors discussed the results and approved the final version of the manuscript.

Competing interests

The authors declare no competing interests.

Additional information

Supplementary information The online version contains supplementary material available at https://doi.org/10.1038/s41467-025-64875-0.

Correspondence and requests for materials should be addressed to Tao Yang.

Peer review information *Nature Communications* thanks the anonymous reviewers for their contribution to the peer review of this work. A peer review file is available.